RESEARCH ARTICLE | MARCH 07 2024

Captured three-dimensional turbulent behaviors inside cyclones using computational fluid dynamics (CFD) design method

Soen Steven; Pandit Hernowo; Imam Mardhatillah Fajri; Pasymi Pasymi; Elvi Restiawaty; Yazid Bindar

AIP Conf. Proc. 3073, 080002 (2024)
https://doi.org/10.1063/5.0199443

Captured Three-Dimensional Turbulent Behaviors Inside Cyclones Using Computational Fluid Dynamics (CFD) Design Method

Soen Steven[1, 2, a)], Pandit Hernowo[3, b)], Imam Mardhatillah Fajri[2, c)], Pasymi Pasymi[4, d)], Elvi Restiawaty[1, 5, e)], and Yazid Bindar[1, 2, 5, f)]

[1]*Department of Chemical Engineering, Faculty of Industrial Technology, Institut Teknologi Bandung, Bandung 40132, Indonesia*
[2]*Biomass Technology Workshop, Faculty of Industrial Technology, Institut Teknologi Bandung, Sumedang 45363, Indonesia*
[3]*Department of Chemical Engineering, Institut Sains dan Teknologi Al-Kamal, Jakarta Barat 11520, Indonesia*
[4]*Department of Chemical Engineering, Universitas Bung Hatta, Padang 25137, Indonesia*
[5]*Department of Bioenergy Engineering and Chemurgy, Faculty of Industrial Technology, Institut Teknologi Bandung, Sumedang 45363, Indonesia*

[a)]*33019004@mahasiswa.itb.ac.id / soensteven201194@gmail.com;*
[b)]*pan_hernowo@ista.ac.id;*
[c)]*imammardhatillahfajri@gmail.com;*
[d)]*pasymi@bunghatta.ac.id;*
[e)]*elviwibisono@gmail.com;*
[f)]*Corresponding author: ybybyb@itb.ac.id*

Abstract. The behavior of turbulent flow inside cyclones is a complicated matter to study. Fortunately, computational fluid dynamics (CFD) has become a powerful tool for comprehensively digitalizing and visualizing those phenomena. This study, hence, intends to capture and examine the behavior of turbulent flow inside cyclones. They were quantified using the standard k-ε model. The observed variables comprised static pressure, velocity magnitude, flow pathline, turbulent kinetic energy, and turbulent kinetic dissipation rate. The influence of vortex finder depth and inlet width on flow behavior was also scrutinized. According to the results, the greater turbulence of cyclones was generated at a higher inlet air flow rate and shallower vortex finder depth of below 9 cm or above the inlet air location. Although cyclones with a deeper vortex finder depth of more than 19 cm had a better separation performance, the cyclone manufacturing cost should be considered. Apart from that, the inlet width geometry should not be ≥ 15 cm and/or should not be ≤ 3 cm because it resulted in poor gas-solid separation performance. Finally, the standard k-ε model was concluded and proved can reveal the behavior of turbulent flow inside cyclones with logical results and patterns.

INTRODUCTION

Massive dependence on fossil resources to support human life released tremendous CO_2 emissions, which has become a threat to the environment [1–7]. Recent advances in agricultural biomass utilization and valorization have attracted much attention because of their ability to produce chemicals and energy with a lower carbon footprint [8–14]. Indonesian biomass such as bamboo leaves, rice husk, oil palm shell, oil palm frond (midrib), and oil palm empty fruit bunches have been widely utilized through thermochemical routes either by pyrolysis or combustion [15–21].

In order to achieve complete process conversion, the perfect and satisfying heat transfer contact that occurs in the pyrolyzer or combustor must be provided [22–24]. One way that can be realized is by reducing the size of raw materials [25–28]. The biochar produced from biomass pyrolysis as well as the ash produced from biomass combustion of

International Seminar on Chemical Engineering Soehadi Reksowardojo (STKSR) 2022
AIP Conf. Proc. 3073, 080002-1–080002-11; https://doi.org/10.1063/5.0199443
Published by AIP Publishing. 978-0-7354-4872-8/$30.00

course also has a small particle size. They can even be smaller than the size of biomass due to their more brittle structure [29,30].

As a result of this problem, particle handling needs to be taken concern. The least expensive technique is widely solved by installing a cyclone separator at the downstream process [31,32]. It is often used to separate particles from gas. The working principle of the cyclone involves particles and gas flow that enter in a tangential direction. The flow is then pushed downward spirally. Centrifugal and inertial forces cause the particles to collide with the wall and then move down to the bottom of the cyclone [33–35]. Near the bottom of the cyclone, the gas continues to reverse and flow upward in smaller spirals. Clean gas is found at the top of the cyclone while particles are collected at the bottom [36].

Another advantage of using cyclone is that it has no moving parts, low maintenance costs, and can operate in various conditions [27,37–39]. Besides, cyclone is often described as equipment with high efficiency but high operating costs. The high operating costs are because cyclones need a large amount of power to overcome the pressure drop. In addition, in its development, it was noted that cyclone was able to achieve up to 98% efficiency for particles with a diameter of more than 346 microns [40].

In general, the flow that occurs in a cyclone is classified as a complex turbulent flow. However, the turbulent flow behavior inside cyclones is complicated to study. Other than that, research aimed at improving cyclone performance by changing the main geometry and operating conditions is considered to be difficult and expensive due to the trial-error method. Fortunately, computational fluid dynamics (CFD) has become a powerful method for visualizing and studying those phenomena in cheaper, more efficient, and more comprehensive ways [41–47].

The study on cyclone performance improvement is mainly realized by variating vortex finder geometry, inlet dimension and orientation, conical geometry, cone tip dimension, and cyclone height [31,32]. Research on the effect of changing the inflow angle of 45^{o} on the cyclone body has been carried out numerically using the RSM (Reynolds Stress Model) as a turbulent model. This study showed that there will be an increase in tangential velocity inside the cyclone without an increase in pressure drop by changing the flow angle of 45^{o} to the cyclone body [48]. The review study from Nakhaei et al. about flow and performance in cyclone separator also mentioned that the simulation was mostly conducted using advanced turbulent models which require high computation load, i.e. 5th-order polynomial RSM and LES (Large Eddy Simulation) [44].

Since the research using CFD is mostly realized with advanced and intensive computation load of turbulent models, this present study intends to employ the simple turbulent model (standard k-ε) to study the flow behavior in cyclones. Still, the effects of vortex finder depth and inlet width in cyclone performance using CFD technique with standard k-ε model are still rare to communicate. This study also aimed to investigate the effects of vortex finder depth and inlet width on three-dimensional turbulent flow behavior for 5 types of cyclones. The profile of static pressure, velocity magnitude, flow pathline, turbulent kinetic energy, and turbulent kinetic dissipation rate inside cyclones was captured and scrutinized.

INVESTIGATION METHODOLOGY

Geometry and Simulation Problem

The study was related to the flow in a cyclone separator with inlet flow rate of 3 m/s. The main cyclone is named "S1" with the following geometry as follows: D = 30 cm; W = 7 cm; H = 18 cm; S = 19 cm (+ 14,5 cm upward); D_d (spigot area) = 18 cm; L_b = 48 cm; L_c = 78 cm; D_e = 12 cm; H = 126 cm; and inlet length = 50 cm. There were also other 4 types of cyclone with the main geometries similar to S1 but has several modifications as follows: cyclone "S2" with S = 49 cm and W = 7 cm; cyclone "S3" with S = 6 cm and W = 7 cm; cyclone "S4" with S = 19 cm and W = 15 cm; and cyclone "S5" with S = 19 cm and W = 3 cm. In other words, cyclone S2 has a deeper vortex finder depth than cyclone S1; cyclone S3 has a shallower vortex finder depth than cyclone S1; cyclone S4 has a wider inlet width than cyclone S1; and the S5 cyclone has a narrower inlet width than cyclone S1. The sketch and geometry of the main cyclone are given in Figure 1.

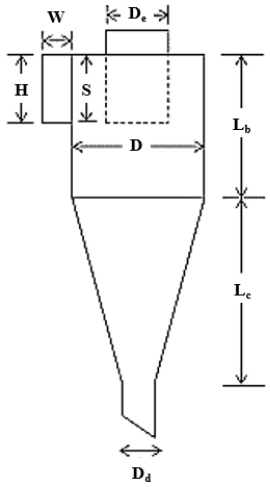

FIGURE 1. Sketch and geometry of the main cyclone.

Mathematical Model Description (Governing Equations)

The study used the standard k-ε model since it has the lowest computational load as well as is widely applied in engineering problems [49,50]. It comprised of mass conservation equation as in equation 1 and momentum conservation equation as expressed in equation 2. Both equations involved fluid density (ρ), fluid viscosity (μ), static pressure (p), and gravity acceleration constant (g). Turbulent viscosity (μ_t) is then described in the forms of turbulent kinetic energy (k) and turbulent kinetic dissipation rate (ε) terms, following equation 3 [51–55]. In addition, k variable is specified in equation 4 and equation 5 is associated with ε variable [45,49,56].

$$\frac{\partial \rho}{\partial t} + \sum_{i=x}^{y,z} \frac{\partial (\rho \overline{u_i})}{\partial i} = 0 \tag{1}$$

$$\rho \frac{\partial \overline{u_x}}{\partial t} + \sum_{i=x}^{y,z} \left[\overline{u_i} \frac{\partial (\rho \overline{u_x})}{\partial i} \right] = -\frac{\partial \bar{p}}{\partial x} + \sum_{i=x}^{y,z} \left\{ \frac{\partial}{\partial i} \left[(\mu + \mu_t) \frac{\partial (\rho \overline{u_x})}{\partial i} \right] \right\} + \rho g_x \tag{2a}$$

$$\rho \frac{\partial \overline{u_y}}{\partial t} + \sum_{i=x}^{y,z} \left[\overline{u_i} \frac{\partial (\rho \overline{u_y})}{\partial i} \right] = -\frac{\partial \bar{p}}{\partial y} + \sum_{i=x}^{y,z} \left\{ \frac{\partial}{\partial i} \left[(\mu + \mu_t) \frac{\partial (\rho \overline{u_y})}{\partial i} \right] \right\} + \rho g_y \tag{2b}$$

$$\rho \frac{\partial \overline{u_z}}{\partial t} + \sum_{i=x}^{y,z} \left[\overline{u_i} \frac{\partial (\rho \overline{u_z})}{\partial i} \right] = -\frac{\partial \bar{p}}{\partial z} + \sum_{i=x}^{y,z} \left\{ \frac{\partial}{\partial i} \left[(\mu + \mu_t) \frac{\partial (\rho \overline{u_z})}{\partial i} \right] \right\} + \rho g_z \tag{2c}$$

$$\mu_t = 0.09 \rho \frac{k^2}{\varepsilon} \tag{3}$$

$$\rho \frac{\partial k}{\partial t} + \sum_{i=x}^{y,z} \left[\overline{u_i} \frac{\partial (\rho k)}{\partial i} \right] = \sum_{i=x}^{y,z} \left\{ \frac{\partial}{\partial i} \left[\left(\mu + \frac{\mu_t}{1.0} \right) \frac{\partial k}{\partial i} \right] \right\} + G_k - Y_k \tag{4a}$$

$$G_k = 2\mu_t \sum_{i=x}^{y,z} \left[\left(\frac{\partial \overline{u_i}}{\partial i} \right)^2 \right] + \mu_t \sum_{i=x}^{y,z} \sum_{j=y}^{z,x} \left[\left(\frac{\partial \overline{u_i}}{\partial j} + \frac{\partial \overline{u_j}}{\partial i} \right)^2 \right] \tag{4b}$$

$$Y_k = \rho \varepsilon \tag{4c}$$

$$\rho \frac{\partial \varepsilon}{\partial t} + \sum_{i=x}^{y,z} \left[\overline{u_i} \frac{\partial (\rho \varepsilon)}{\partial i} \right] = \sum_{i=x}^{y,z} \left\{ \frac{\partial}{\partial i} \left[\left(\mu + \frac{\mu_t}{1.3} \right) \frac{\partial \varepsilon}{\partial i} \right] \right\} + 1.44 \frac{\varepsilon}{k} G_k - 1.92 \rho \frac{\varepsilon^2}{k} \tag{5}$$

Numerical Procedure and Solution Settings

The disclosed problem was solved numerically using ANSYS Fluent 2021. A tetrahedral grid cell was generated to a number of 1,500,000 due to the optimal grid size that still compensates for medium computational load [42,45,50]. A coupled algorithm of the steady-state solving method was used for pressure velocity coupling. The spatial discretization methods consist of gradient (based on least square cell method), momentum (using 2nd order upwind method), pressure (using 2nd order method), as well as k and ε (using 1st order upwind method) [49]. The pseudo-transient explicit relaxation factors were 0.5 for pressure, 0.5 for momentum, 1 for density, 1 for body forces, 0.75 for k, 0.75 for ε, and 1 for μ_t [49]. The residual absolute criteria were set at 10^{-6} to guarantee convergence. The numerical calculation was performed at 1000 iterations.

RESULTS AND DISCUSSION

Model Validation

The standard k-ε model was initially validated using the experiment by Hoekstra (2000). It was chosen since his experiment dealt with air and particle flow in a cyclone separator [57] which is a somewhat similar case compared with this study. His cyclone had main diameter of 29 cm; total height of 116 cm; height for cone section of 72.5 cm; spigot diameter of 10.8 cm; vortex finder with a diameter of 14.5 cm, height of 29 cm, and half of the height sank into the main cyclone chamber; inlet width of 5.8 cm; and inlet height of 14.5 cm. The air flew in such a way had a Reynold number of 280,000. Boundary conditions at inlet and outlet locations had turbulent intensity of 10% and length scale ratio of 0.7 [57]. The investigated parameter was the total pressure drop between inlet and outlet of the cyclone.

The simulation for model validation was carried out under RNG k-ε model, realizable k-ε model, and SST-k-ω model. All of the results were compared and were then summarized in Table 1. From all models, SST-k-ω gave the closest result compared to the experiment (difference percentage 4.82%) and then followed by the standard k-ε model (difference percentage 4.35%). Nevertheless, the standard k-ε model provided the lowest computation load so it requires the shortest computation time [49,50,58,59]. Hence, this model was confidently selected to be used for this study.

TABLE 1. Total pressure drop inside the cyclone under several turbulent models.

Turbulent Models	Total Pressure Drop		
	Experiment	Simulation	Difference
Standard k-ε	590.8 Pa	562.3 Pa	4.82%
RNG k-ε	590.8 Pa	659.6 Pa	11.64%
Realizable k-ε	590.8 Pa	524.3 Pa	11.26%
SST-k-ω	590.8 Pa	565.1 Pa	4.35%

Contours of Air Flow in Cyclones S1-S5

The highest pressure was located at the wall area and its value became lower until reaching the vacuum at the center position for all types of cyclones, as depicted in Figure 2. This phenomenon compelled the tangential flow to move to the center and then flow out of the cyclone as the effect of the centripetal force [32,37,60]. The most vacuum condition lay in the bottom area of the vortex finder (point "X"). The cyclone with the slightest vacuum area was S4 because of its widest cross-sectional inlet area which reflects the largest velocity magnitude (Figure 2d), but it had a high possibility to drag the particle out (particle entrainment). In contrast, cyclone S5 had the lowest velocity magnitude so it created the broadest vacuum area inside the cyclone as seen in Figure 2e. Unfortunately, the broader vacuum area inside the cyclone led to a high potential for solid suction flow to the center which resulted in poor gas-solid separation performance [60,61]. This section implied that inlet width geometry should not be ≥ 15 cm and/or should not be ≤ 3 cm.

Meanwhile, the velocity magnitude inside the cyclone was zero in all wall positions in the blue zone as shown in Figure 3. The highest velocity for S4 cyclone was located at the vortex finder which is indicated by the red parabolic area (Figure 3d) whereas the highest velocity for other cyclones was located at the annulus area. In Figure 3, the zero velocity at the center of the cyclone happened because it had no linear flow passing through this area but in the form of spiraling or vortexing flow [62]. This phenomenon was strongly confirmed by the flow pathline profiles in Figure 4. This was similar to the air trajectories from CFD study of the Bohnet cyclone by Gimbun et al. [63]. The figure also augmented that air inlet first tangentially flowed along the wall (reflected by outer vortices with a descending flow) until reaching spigot and then it rose up to flow out through the vortex finder (represented by inner vortices with an ascending flow) [28,32].

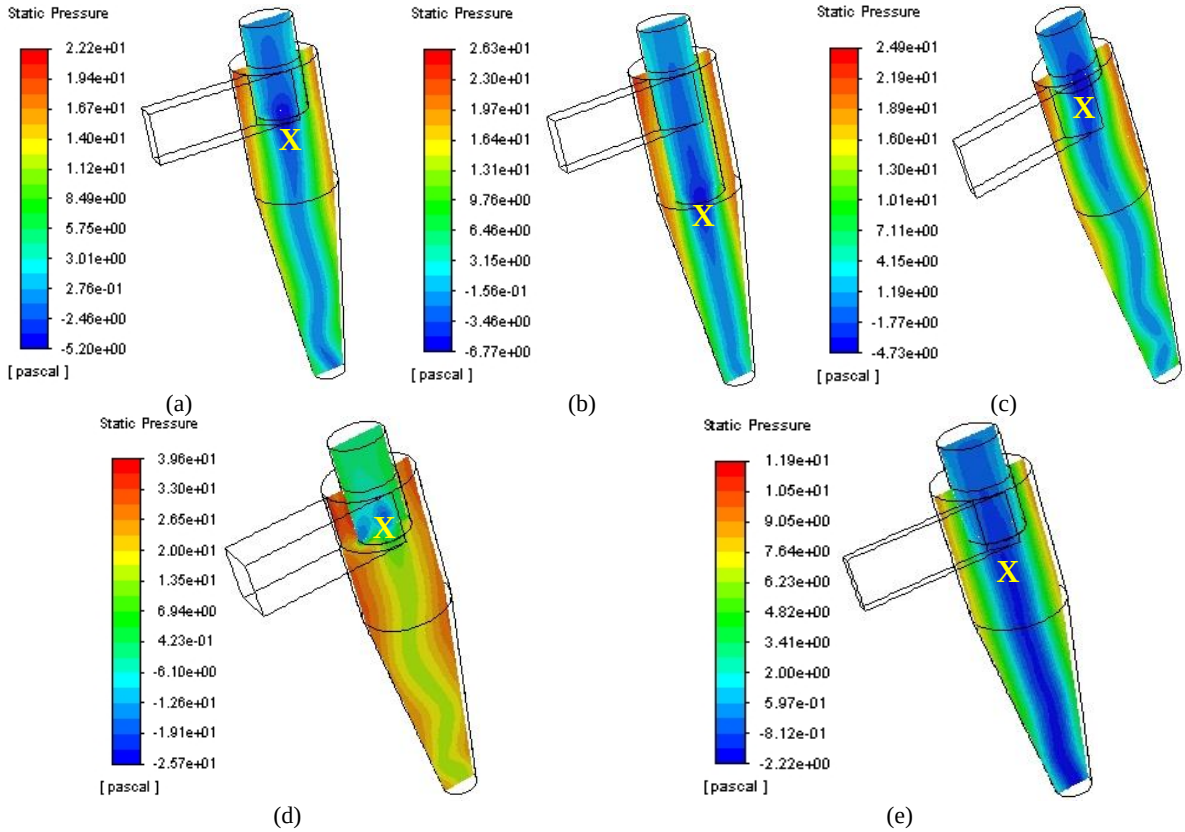

FIGURE 2. Profile of the static pressure in cyclone S1 (a), S2 (b), S3 (c), S4 (d), and S5 (e).

As served in Figure 5, the turbulent kinetic energy achieved maximum values at the bottom area or entrance of vortex finder (red zone). Interestingly, those values drastically dropped to the order of 10^{-2}-10^{-4} m^2/s^2 (blue zone) at the wall due to laminarization [64,65]. Turbulence was more intense when flow passes the location with area change and/or area with obstructions. The narrowing area from inside the cyclone main chamber to the outlet pipe enhanced the velocity of the fluid and it consequently generated higher turbulence [66]. Cyclone S3 had a broader turbulence area at the annulus as served in Figure 5c. It was caused by the unification of turbulence from the inlet air flow with turbulence generated by the vortex finder. This affected poor gas-solid separation performance because the entering flow can be disturbed by the ascending vortexing flow and this led to the particle entraining out from the cyclone. Therefore, shortening the vortex finder depth of below 9 cm to a position above the inlet pipe location was not recommended to be chosen.

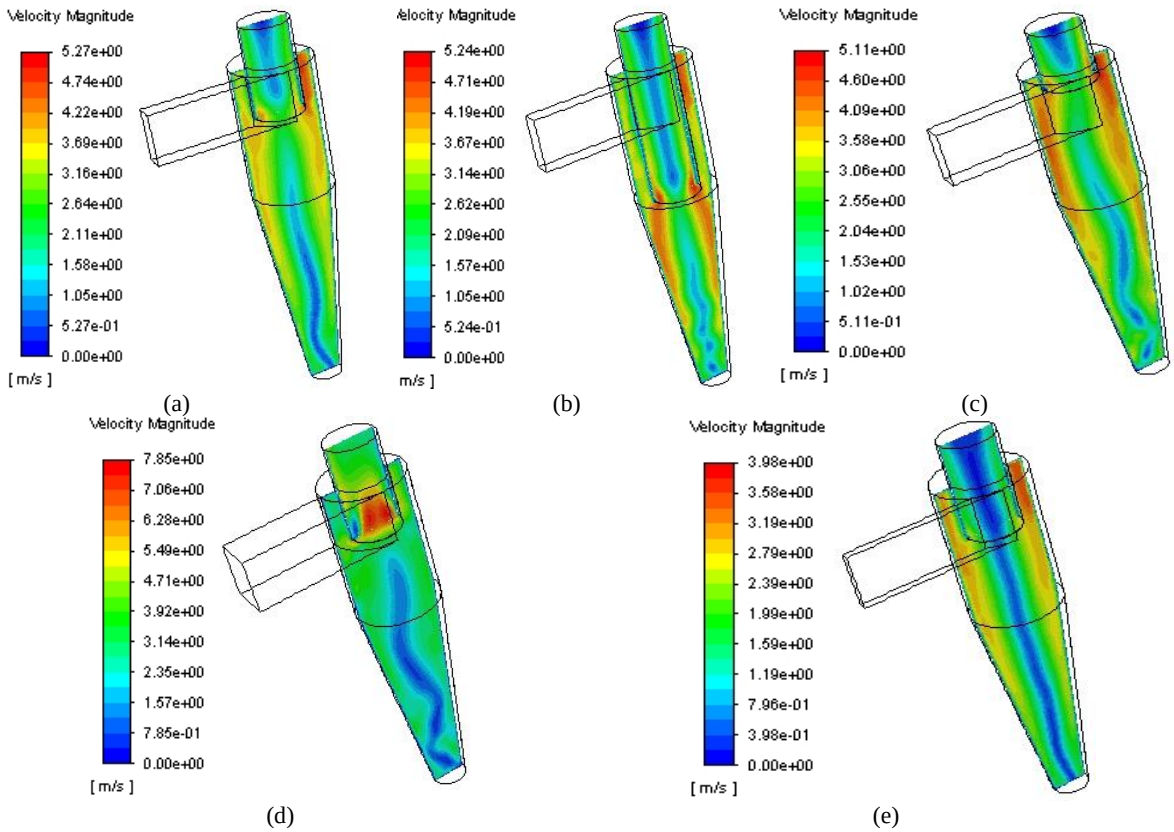

FIGURE 3. Profile of the velocity magnitude in cyclones S1 (a), S2 (b), S3 (c), S4 (d), and S5 (e).

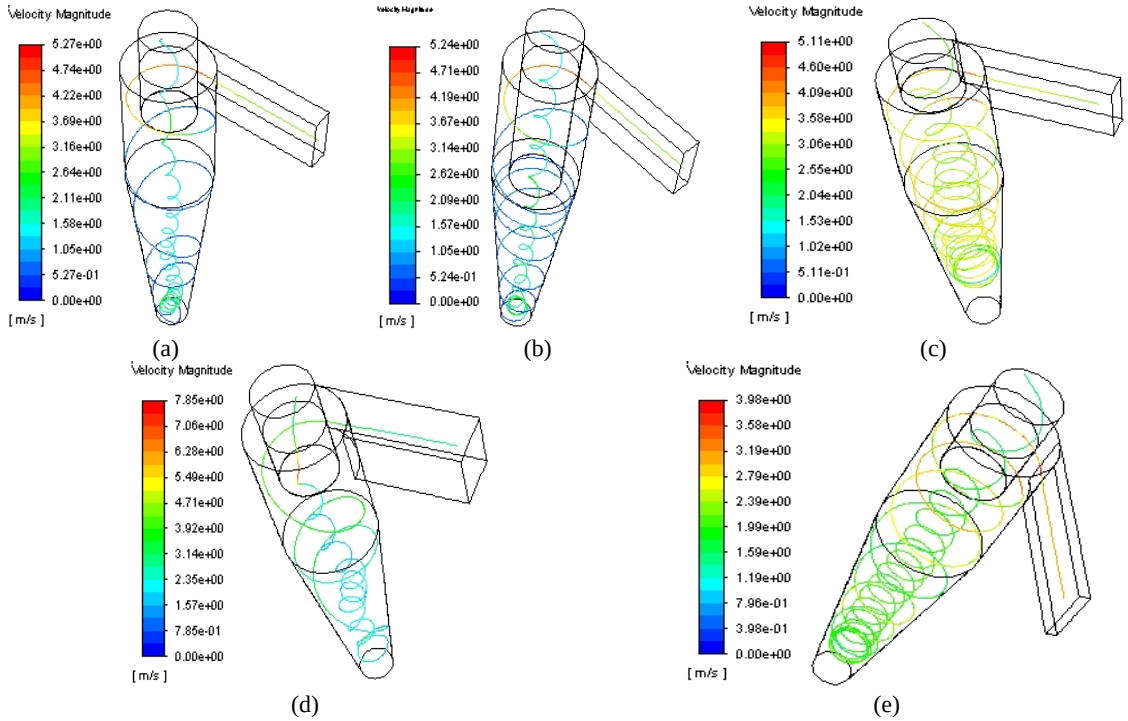

FIGURE 4. Flow pathline in cyclones S1 (a), S2 (b), S3 (c), S4 (d), and S5 (e).

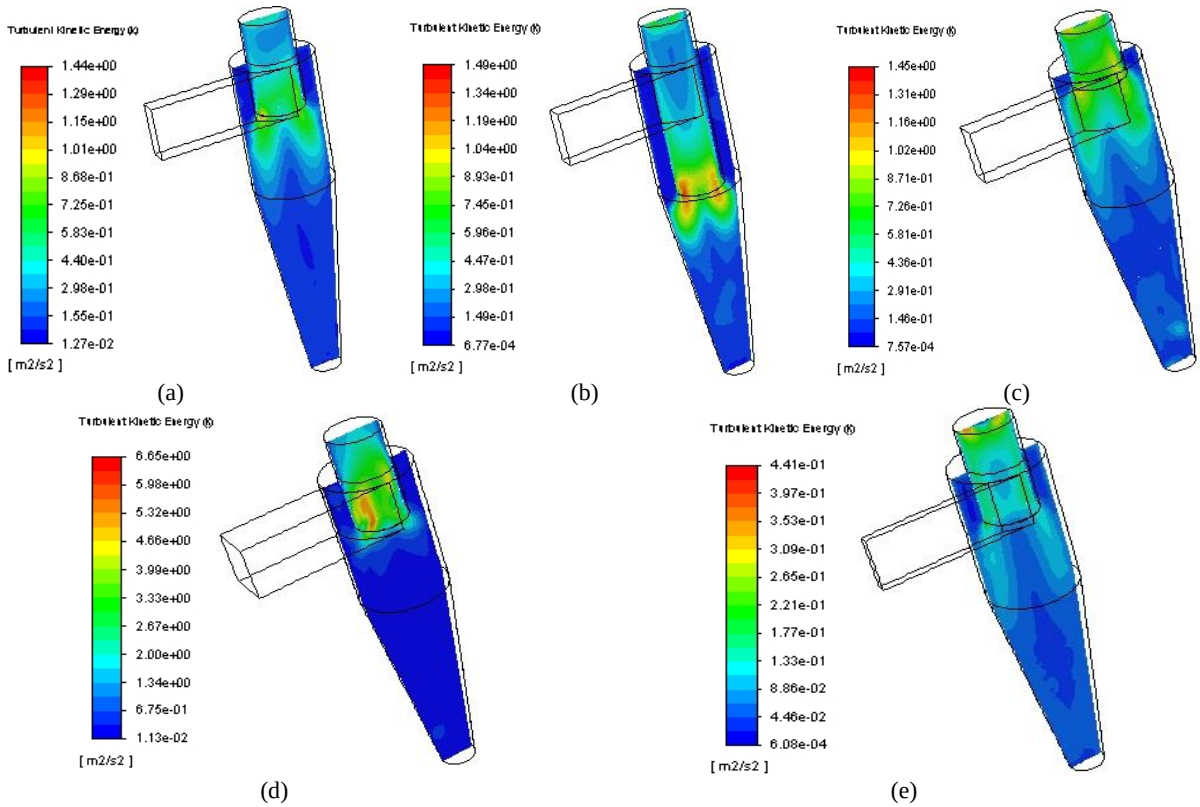

FIGURE 5. Profile of the turbulent kinetic energy in cyclones S1 (a), S2 (b), S3 (c), S4 (d), and S5 (e).

Analysis of Cyclonic Flow Profile in the Radial Position

The profiles at the radial position for all cyclones at a height of 1.2 m showed the existence of two different zones, namely vortex finder zone and annulus zone. The separation of those two zones was indicated by a purple line. Figure 6 revealed somewhat similar values of static pressure for cyclones S1-S3. The lowest value of static pressure was nominated for cyclone S5 while the largest is for S4. Furthermore, the pressure in the vortex finder was lower than the annulus, for all cyclones. This was consistent with the previous explanation that flow tends to move to the center and then flow out of the cyclone as the effect of the centripetal force [32,37,60].

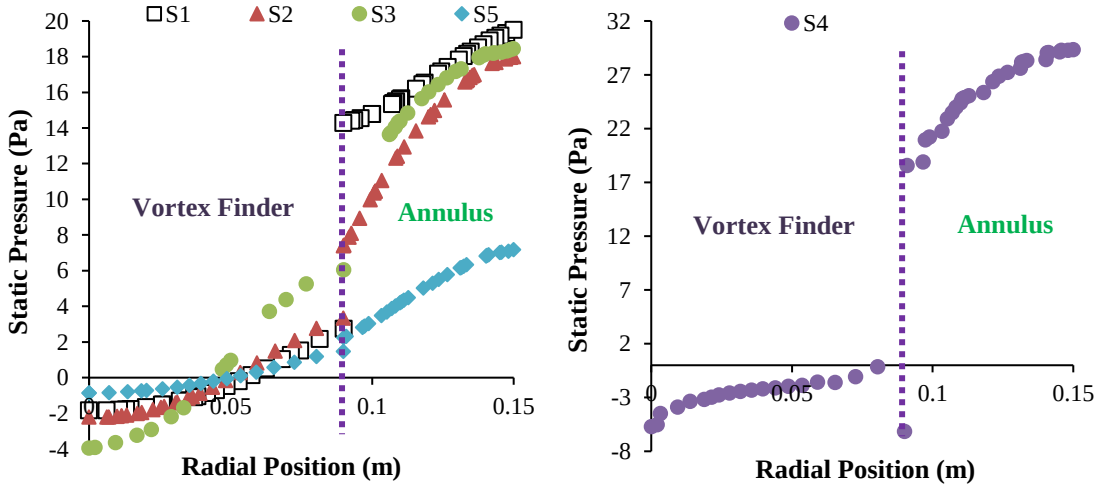

FIGURE 6. Plots of the static pressure of cyclones in the radial position.

Based on Figure 7, the maximum velocity magnitude was located at the position as long as not at the wall area of both vortex finder and annulus. Meanwhile, the velocity at the wall had a low velocity and then becomes zero due to laminarization [64,65]. This figure reinforced that cyclone S4 had the largest velocity magnitude, whereas cyclone S5 had the lowest value. In addition, the turbulent kinetic energy of the cyclones was presented in Figure 8. It can be seen that turbulent kinetic energy in the vortex finder was greater than the annulus. Along the radial direction, the turbulent kinetic energy increased gently, then drastically dropped at the outlet wall area, and finally discontinued when enters the annulus. Likewise, the turbulent kinetic energy was found to have a greater value in cyclone S4 due to the highest velocity magnitude and the value became lessening in cyclone S5 because of its smallest air inlet velocity.

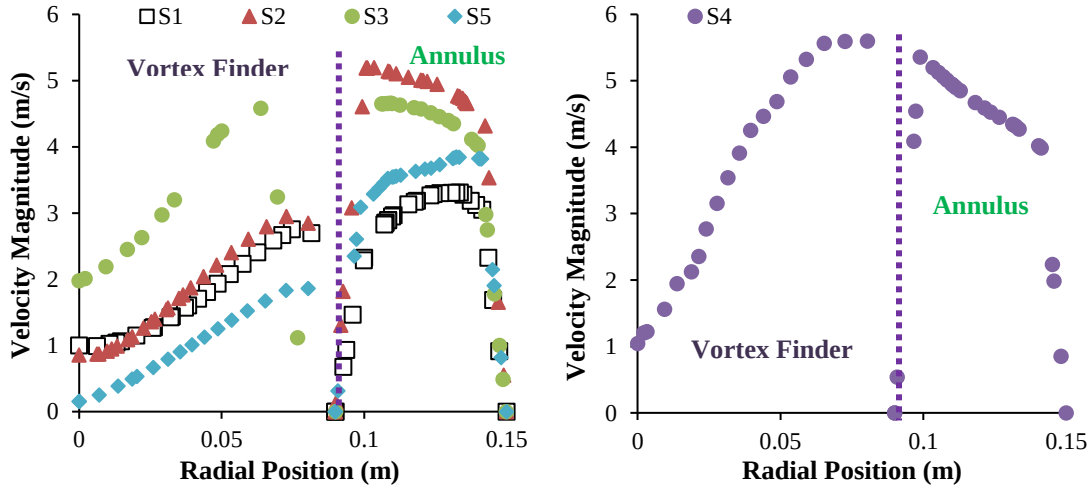

FIGURE 7. Plots of the velocity magnitude of cyclones in the radial position.

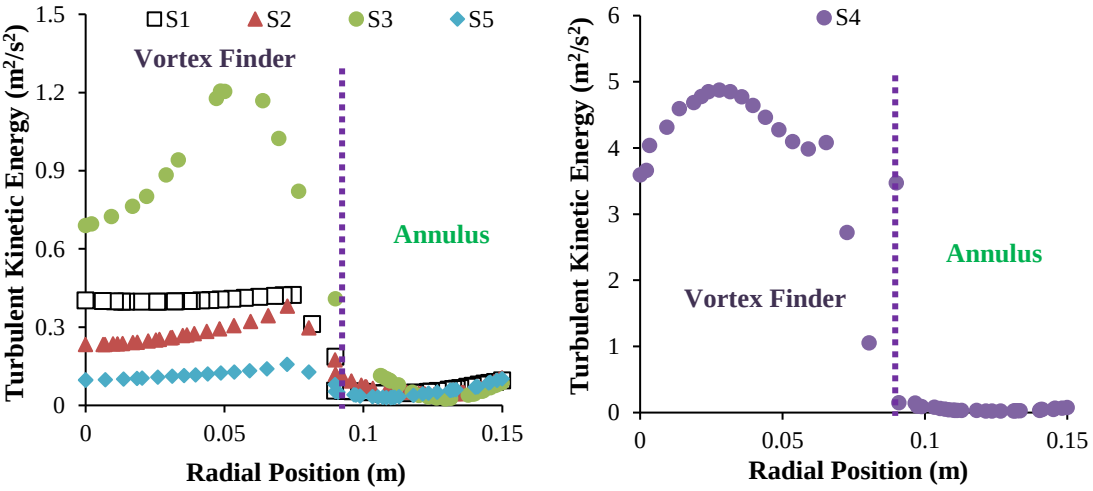

FIGURE 8. Plots of the turbulent kinetic energy of cyclones in the radial position.

On the other hand, Figure 9 exhibited that the turbulent kinetic dissipation rate drastically increased, especially at the wall of vortex finder and cyclone because of laminarization near the wall [64,65,67,68]. The turbulence variables for cyclone S3 appeared to be greater than S1 and S2 due to the mixing between the fluid entering cyclone and the fluid that is about to exit the cyclone. The same pattern for turbulent kinetic dissipation rate and turbulent kinetic energy caused the highest value for ε to be nominated to cyclone S4 and the lowest value is for cyclone S5. The plot of profiles in the radial position confirmed that shortening the vortex finder depth of below 9 cm to a position above the inlet air location was not recommended to be chosen. In contrast, although the deeper vortex finder depth can enhance the separation performance [39], it leads to a high cyclone manufacturing cost.

CONCLUSION

The computational fluid dynamics (CFD) method has proven to be a promising tool for capturing 3D turbulent behaviors inside cyclones. According to the five cyclones simulated, the air will first tangentially flow along the wall until reaching spigot and then it rises up to flow out through the vortex finder. Afterward, cyclones with a vortex finder depth of more than 19 cm have a better separation performance. Contrary, vortex finder depth below 9 cm caused the unification of turbulence from the inlet air flow with turbulence generated by the vortex finder which lessens gas-solid separation performance. Other than that, the inlet width of ≥ 15 cm and/or ≤ 3 cm will also result in poor separation performance. From this study, the standard k-ε model is concluded that can exhibit the behavior of turbulent flow inside cyclones with logical results and patterns.

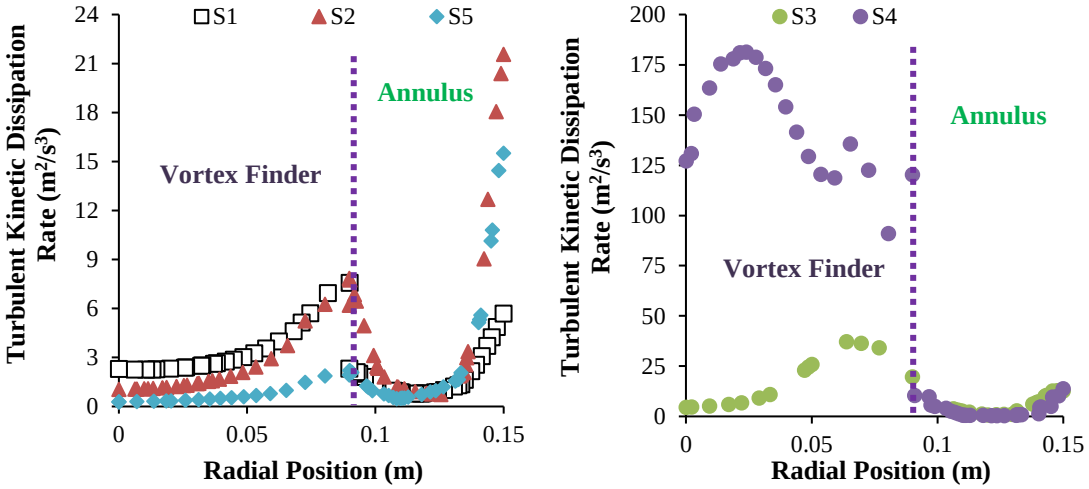

FIGURE 9. Plots of the turbulent kinetic dissipation rate of cyclones in the radial position.

REFERENCES

1. I. Quispe, R. Navia, and R. Kahhat, Waste Manag. **59**, 200–210 (2017).
2. S. Steven, D. L. Friatnasary, A. K. Wardani, K. Khoiruddin, G. Suantika, and I. G. Wenten, IOP Conf. Ser.: Earth Environ. Sci. **963**, 012034 (2022).
3. D. K. Sarkar, "Fuels and combustion", in *Thermal Power Plant Design and Operation*, edited by D. K. Sarkar, 1st ed. (Elsevier, 2015), pp. 91–137.
4. S. Ependi and T. B. Nur, IOP Conf. Ser:. Mater. Sci. Eng. **309**, 1–7 (2018).
5. P. Hernowo, S. Steven, E. Restiawaty, and Y. Bindar, J. Taiwan Inst. Chem. Eng. **139**, 104520 (2022).
6. T. Chungsangunsit, S.H. Gheewala, and S. Patumsawad, Int. J. Energy Environ. Eng. **3**, 625–630 (2009).
7. T. Chungsangunsit, S.H. Gheewala, and S. Patumsawad, Int. Energy J. **6**, 347–355 (2005).
8. W. Dessie, X. Luo, M. Wang, L. Feng, Y. Liao, Z. Wang, Z. Yong, and Z. Qin, Appl. Microbiol. Biotechnol. **104**, 4757–4770 (2020).
9. T. D. Searchinger, T. Beringer, B. Holtsmark, D. M. Kammen, E. F. Lambin, W. Lucht, P. Raven, and J. P. Van-Ypersele, Nat. Commun. **9**, 1–4 (2018).
10. S. Pang, Biotechnol. Adv. **37**, 589–597 (2019).
11. Y. Bindar, S. Steven, S. W. Kresno, P. Hernowo, E. Restiawaty, R. Purwadi, and T. Prakoso, Biomass Conv. Bioref. (2022).
12. E. Johnson, Environ. Impact Assess. Rev. **29**, 165–168 (2009).
13. S. Madusari, S. S. Jamari, N. I. A. A. Nordin, Y. Bindar, T. Prakoso, E. Restiawaty, and S. Steven, ChemBioEng Rev. **10**, 37–54 (2023).
14. E. Restiawaty, Y. Bindar, K. Syukri, O. Syahroni, S. Steven, R. A. Pramudita, and Y. W. Budhi, Biomass Conv. Bioref. (2022).
15. Y. Ramli, S. Steven, E. Restiawaty, and Y. Bindar, Bioenerg. Res. **15**, 1918–1926 (2022).
16. J. Werther, M. Saenger, E. U. Hartge, T. Ogada, and Z. Siagi, Prog. Energy Combust. Sci. **26**, 1–27 (2000).
17. A. Demirbas, Prog. Energy Combust. Sci. **30**, 219–230 (2004).

18. S. Steven, E. Restiawaty, and Y. Bindar, J. Eng. Technol. Sci. **54**, 220304 (2022).
19. S. Steven, P. Hernowo, E. Restiawaty, A. Irawan, C. B. Rasrendra, A. Riza, and Y. Bindar, Waste Biomass Valor. **13**, 2735–2747 (2022).
20. I. J. Fernandes, D. Calheiro, A. G. Kieling, C. A. M. Moraes, T. L. A. C. Rocha, F. A. Brehm, and R. C. E. Modolo, Fuel **165**, 351–359 (2016).
21. S. Steven, E. Restiawaty, and Y. Bindar, Waste Biomass Valor. (2022).
22. S. M. Selvam, T. Janakiraman, and B. Paramasivan, Mater. Today Proc. **47**, 312–317 (2021).
23. N. L. Panwar, A. Pawar, and B. L. Salvi, SN Appl. Sci. **1**, 1–9 (2019).
24. K. Sirisomboon and P. Laowthong, Appl. Therm. Eng. **147**, 718–727 (2019).
25. S. Steven, E. Restiawaty, and Y. Bindar, IOP Conf. Ser.: Earth Environ. Sci. **963**, 012050 (2022).
26. O. Levenspiel, in *Chemical Reaction Engineering, Third Edition* (John Wiley & Sons, 1999), pp. 566–586.
27. M. Marinuc and F. Rus, Bull. Transilv. Univ. Braşov **4**, 117–122 (2011).
28. K. W. Chu, J. Chen, B. Wang, A. B. Yu, A. Vince, G. D. Barnett, and P. J. Barnett, Powder Technol. **320**, 594–609 (2017).
29. P. Basu, *Biomass Gasification, Pyrolysis and Torrefaction* (Elsevier, 2013).
30. J. D. Martínez, T. Pineda, J. P. López, and M. Betancur, Energy **36**, 3846–3854 (2011).
31. P. Zhang, G. Chen, J. Duan, and W. Wang, Sep. Purif. Technol. **210**, 231–235 (2019).
32. J. Duan, S. Gao, Y. Lu, W. Wang, P. Zhang, and C. Li, Adv. Powder Technol. 1–13 (2020).
33. M. Azadi, M. Azadi, and A. Mohebbi, J. Hazard. Mater. **182**, 835–841 (2010).
34. M. Azadi and M. Azadi, Powder Technol. **217**, 121–127 (2012).
35. N. Gopani and A. Bhargava, Int. J. Environ. Sci. Dev. **2**, 350–354 (2011).
36. A. Horvath, C. Jordan, and M. Harasek, Chem. Prod. Process Model. **3**, 1–28 (2008).
37. P. A. Funk and K. D. Baker, J. Cotton Sci. **17**, 40–51 (2013).
38. S. S. Gawali and M. B. Bhambere, Int. J. Mech. Eng. Robot. Res. **4**, 244–248 (2015).
39. A. Surjosatyo, A. Respati, H. Dafiqurrohman, and Muammar, Procedia Eng. **170**, 154–161 (2017).
40. P. A. Funk, S. E. Hughs, and G. A. Holt, J. Cotton Sci. **4**, 178–182 (2000).
41. N. Sylvia, R. Mutia, Malasari, R. Dewi, Y. Bindar, and Yunardi, IOP Conf. Ser:. Mater. Sci. Eng. **536**, 012042 (2019).
42. S. Steven, E. Restiawaty, P. Pasymi, and Y. Bindar, Powder Technol. **410**, 117883 (2022).
43. I. Istadi and Y. Bindar, Appl. Therm. Eng. **73**, 1129–1140 (2014).
44. M. Nakhaei, B. Lu, Y. Tian, W. Wang, K. Dam-Johansen, and H. Wu, Processes **8**, 1–26 (2020).
45. S. Steven, E. Restiawaty, P. Pasymi, I.M. Fajri, and Y. Bindar, Asia-Pac. J. Chem. Eng. **17**, e2805 (2022).
46. P. Pasymi, Y. W. Budhi, and Y. Bindar, ARPN J. Eng. Appl. Sci. **12**, 5300–5306 (2017).
47. E. Balestrin, R. K. Decker, D. Noriler, J. C. S. C. Bastos, and H. F. Meier, Sep. Purif. Technol. **184**, 54–65 (2017).
48. S. Bernardo, A. P. Peres, and M. Mori, Rev. Eng. Térmica **4**, 18–23 (2005).
49. ANSYS, *ANSYS Fluent Theory Guide 2019 R3* (ANSYS Inc., 2019).
50. S. Steven, E. Restiawaty, P. Pasymi, and Y. Bindar, Braz. J. Chem. Eng. (2022).
51. P. Pasymi, Y. W. Budhi, and Y. Bindar, Jurnal Teknologi **82**, 91–100 (2020).
52. P. Pasymi, Y .W. Budhi, and Y. Bindar, ASEAN J. Chem. Eng. **20**, 88–98 (2020).
53. P. Pasymi, Y .W. Budhi, A. Irawan, and Y. Bindar, J. Mech. Eng. Sci. **12**, 4300–4328 (2018).
54. P. Pasymi, Y .W. Budhi, and Y. Bindar, J. Eng. Technol. Sci. **50**, 684–697 (2018).
55. P. Pasymi, Y .W. Budhi, and Y. Bindar, J. Phys.: Conf. Ser. **1090**, 1–8 (2018).
56. G. Maitlo, I. N. Unar, R. B. Mahar, and K. M. Brohi, Energy Explor. Exploit. **37**, 1073–1097 (2019).
57. A. J. Hoekstra, "Gas Flow Field and Collection Efficiency of Cyclone Separators," Ph.D. Thesis, Technische Universiteit Delft, 2000.
58. L. S. Brar, R. P. Sharma, and K. Elsayed, Powder Technol. **286**, 668–677 (2015).
59. S. Wang, H. Li, R. Wang, X. Wang, R. Tian, and Q. Sun, Adv. Powder Technol. **30**, 227–239 (2019).
60. J. Wei, H. Zhang, Y. Wang, Z. Wen, B. Yao, and J. Dong, Powder Technol. **308**, 178–192 (2017).
61. S. C. Chine and J. H. Bhangale, Int. Res. J. Eng. Technol. **5**, 1–4 (2018).
62. J. Ko, "Numerical Modelling of Highly Swirling Flows in a Cylindrical Through-Flow Hydrocyclone," Ph.D. Thesis, Royal Institute of Technology Department of Mechanics, 2005.
63. J. Gimbun, T. G. Chuah, T. S. Y. Choong, and A. Fakhru'l-Razi, Int. J. Comput. Methods Eng. Sci. Mech. **6**, 161–168 (2005).
64. M. Pashtrapanska, J. Jovanović, H. Lienhart, and F. Durst, Exp. Fluids **41**, 813–827 (2006).

65. B. Shome, Int. J. Therm. Sci. **159**, 106597 (2021).
66. C. J. Geankoplis, “Principles of Momentum Transfer and Applications”, in Transport Processes and Unit Operations, Third Edition (Prentice-Hall International, 1993), pp. 114–118.
67. H. A. Vaidya, Ö. Ertunç, B. Genç, F. Beyer, Ç. Köksoy, and A. Delgado, J. Phys.: Conf. Ser. **318**, 1–10 (2011).
68. M. Dohnal and J. Hájek, Chem. Eng. Trans. **52**, 757–762 (2016).